Rotational Instabilities in Post–Collapse Stellar Cores

J. David Brown

Department of Physics, North Carolina State University, Raleigh, NC 27695-8202

Abstract. A core–collapse supernova might produce large amplitude gravitational waves if, through the collapse process, the inner core can aquire enough rotational energy to become dynamically unstable. In this report I present the results of 3-D numerical simulations of core collapse supernovae. These simulations indicate that for some initial conditions the post–collapse inner core is indeed unstable. However, for the cases considered, the instability does not produce a large gravitational–wave signal.

INTRODUCTION

Core–collapse supernovae are potentially rich sources of gravitational waves. When a rotating stellar core exhausts its nuclear fuel the matter in the polar regions collapses more rapidly than the matter in the equatorial plane, since the latter must fight harder against centrifugal forces as it spirals inward. The changing oblateness of the core during this infall phase, and the subsequent changes due to core bounce, will generate gravitational waves (see, for example, Refs. [1,2]). After core bounce convective instabilities will cause the hot neutron star to boil [3], and the resulting convective motions will give rise to a gravitational–wave signal [4]. To a lesser extent, the same boiling process and release of gravitational waves can occur in the neutrino–heated material interior to the shock wave [4]. The supernova explosion itself may have a preferred direction, as evidenced by the large kick velocities of many neutron stars [5]. Such an asymmetry will generate a gravitational–wave signal with memory [6]. Perhaps the most interesting possibility, and the one discussed in this paper, is that the stellar core will spin up as it collapses and produce a very rapidly rotating neutron star. The neutron star might be subject to dynamical instabilities that act to deform, or even fragment the star, and in the process produce large amplitude gravitational waves.

In this paper I present the results of numerical simulations aimed at determining the types of initial conditions for a pre–collapse stellar core that lead to a dynamically unstable post–collapse inner core. The only previous investigations along these lines is found in the work of Rampp, Müller, and Ruffert [7].

Analytical and numerical work on rapidly rotating fluid stars with Maclaurin–like rotational laws has shown that dynamical instabilities, in particular the $m = 2$ bar–mode instability, will grow when the stability parameter $T/|W|$ (the ratio of rotational kinetic energy to gravitational potential energy) exceeds about 0.27 [8]. For certain angular velocity profiles, a dynamical $m = 1$ instability can grow for $T/|W|$ as low as ~ 0.14 [9]. A back–of–the–envelope calculation frequently quoted in the literature suggests that the stability parameter will scale as $T/|W| \sim 1/R$ during collapse, where R is the radius of the core. For a 10 solar mass star whose core collapses completely to neutron star size, this implies a factor ~ 100 increase in $T/|W|$. Based on this argument, one would expect that even the most slowly rotating cores will be dynamically unstable after collapse.

The factor ~ 100 increase in $T/|W|$ is overly optimistic for two reasons. First, centrifugal forces can halt the collapse at subnuclear density, producing a bloated inner core with $T/|W|$ below the threshold for dynamical instability. Second, the core actually "implodes", rather than collapses, and some of the stellar core's matter and angular momentum remain outside the inner core. Since only a percentage of the core's angular momentum is drawn into the inner core, the increase in rotational kinetic energy is less than one would predict by assuming a more complete collapse. On the other hand, the simulations described here provide evidence that the entire core need not have $T/|W| \gtrsim 0.27$ for the bar mode to grow on a relatively short timescale. It might be possible for the bar instability to grown as a secular process on a timescale of a few rotation periods, due to coupling between the inner and outer core regions.

Two of the most rapidly rotating pre–collapse models considered here lead to dynamically unstable post–collapse inner cores. These models are unstable to the $m = 2$ bar mode, but the resulting bars have insufficient density and spatial extent to generate large gravitational–wave signals. In both cases, the contribution to the gravitational–wave signal from the bar deformation is smaller in amplitude, by a factor of $\sim$ 2–5, than the purely axisymmetric signal generated by the core's changing oblateness during collapse and bounce. Overall, for sources in the Virgo cluster, these signals are too weak to be detected by laser interferometers operating in broadband mode. For galactic sources, these signals should be detectable.

NUMERICAL CODE AND INITIAL MODELS

The numerical code used for these investigations was written in collaboration with John Blondin. It uses Newtonian hydrodynamics and Newtonian gravity, ignores neutrino heating and cooling, and uses the relatively simple analytical equation of state discussed by Zwerger and Müller [2,7]. The gravitational–wave signal is computed in the quadrupole approximation. The hydrodynamical equations are solved with VH-1, written by Blondin, J. Hawley, G. Lindahl, and E. Lufkin. VH-1 uses the piecewise parabolic method [10]. The Poisson equation for the gravitational potential is solved with multigrid techniques.

Our code models the supernova in a minimal way, retaining just enough physics to capture the gravitational–wave signal in the leading–order quadrupole approximation. Nevertheless, the computation is a challenge due to the discrepancy in length scales involved. While the stellar core has a radius of 1000's of kilometers, the computational grid must have zone sizes of no more than $\sim 1\,\mathrm{km}$ to support the steep density and velocity gradients in the inner core. A uniform 3-D Cartesian grid would require $\sim 10^{10}$ zones for these simulations, which is not feasible with current technology. One possible solution to this problem is to use a spherical–coordinate grid with non–uniform radial spacing, so the zones are smallest in the inner regions of the grid. The difficulty with this approach is that the zones become too narrow in the angular directions near the coordinate origin, and this drives the Courant–limited timestep to zero. The solution we have adopted is a nested grid scheme, in which the computational domain is covered by a sequence of Cartesian grids with increasing resolution and decreasing size. In this way only the inner–most region is covered with high resolution. This approach was also used by Rampp, Müller, and Ruffert [7]. The simulations described here use 7 grids, each with 64^3 zones.

In addition to the 3-D code just described, I also work with a 2-D code that assumes axisymmetry. The 2-D code uses a system of nested Cartesian grids in the r–z plane to achieve the necessary resolution of the inner core. The 2-D simulations reported here use 6 grids, each with 128^2 zones.

In this paper I consider a sequence of initial models of the pre–collapse stellar core. The goal is to determine which of these models lead to dynamically unstable post–collapse inner cores. Each initial model is a rotating, equilibrium polytrope with $\Gamma = 4/3$ and central density $\rho_c = 10^{10}\,\mathrm{g/cm^3}$. The rotation laws for the sequence are given by

$$\Omega(\varpi) = \Omega_0 e^{-(\varpi/1500\,\mathrm{km})^2}\ , \qquad \Omega_0 = 8,\ 12,\ 16,\ 20,\ 24\,\mathrm{rad/s}, \tag{1}$$

where Ω is the angular velocity and ϖ is the distance from the rotation axis. The Gaussian form for $\Omega(\varpi)$ was motivated in part by the results of Heger, Langer, and Woosley [11]. Their simulations of stellar evolution with rotation yield pre–collapse cores with relatively broad, Gaussian–like angular velocity profiles, similar in shape to the profile (1). Note, however, that even their most rapidly rotating model has an overall scale of $\Omega_0 \approx 10$, somewhat smaller than most of the models (1).

In their previous work Rampp, Müller, and Ruffert [7] used an initial data set with angular velocity profile $\Omega(\varpi) = \Omega_0/[1 + (\varpi/100\,\mathrm{km})^2]$ and $\Omega_0 \approx 140\,\mathrm{rad/s}$. The resulting model is highly differentially rotating. The angular velocity drops from its central value of about $140\,\mathrm{rad/s}$ to less than $4\,\mathrm{rad/s}$ at a distance of $R_{\mathrm{eq}}/2$, where $R_{\mathrm{eq}} \approx 1260\,\mathrm{km}$ is the equatorial radius. By contrast, the angular velocity of the most rapidly rotating model (1) drops from $24\,\mathrm{rad/s}$ to about $13\,\mathrm{rad/s}$ at $R_{\mathrm{eq}}/2$, where $R_{\mathrm{eq}} \approx 2500\,\mathrm{km}$.

The equation of state [2,7] contains a polytropic part whose stiffness depends on whether the matter is below or above nuclear density, and a thermal part that models the thermal pressure of matter heated by shock waves. Collapse of the

initial models is induced by choosing the polytropic index in the sub–nuclear density regime to be $\Gamma = 1.28$, significantly below the value of 4/3 required for the model to remain in equilibrium. Random density perturbations at the 1% level were imposed at the beginning of the 3-D simulations.

RESULTS

The stability parameter is plotted as a function of time in Figure 1 for the sequence of models (1). These simulations were run with the 2-D code. Observe that $T/|W|$ increases by a factor of 2 or less as a result of core collapse. As shown in Figure 2, for the initial models with angular velocity $\Omega_0 = 16$, 20 and 24 rad/s, the core experiences a centrifugal bounce and never reaches nuclear density $\rho_{\rm nuc} = 2.0 \times 10^{14}\,{\rm g/cm^3}$. For the model with $\Omega_0 = 12\,{\rm rad/s}$, the inner core reaches nuclear density at core bounce then relaxes to a central value slightly below nuclear density. Only the most slowly rotating initial data, with $\Omega_0 = 8\,{\rm rad/s}$, forms a stiff inner core with density greater than $\rho_{\rm nuc}$. These results show that centrifugal forces can severely inhibit core collapse, and prevent the stability parameter from experiencing the kind of growth suggested by the back–of–the–envelope arguments discussed in the introduction.

The stability parameter for the two most rapidly rotating models exceeds 0.27 after core bounce. I will use the labels Ω20 and Ω24 to denote the models with $\Omega_0 = 20\,{\rm rad/s}$ and $\Omega_0 = 24\,{\rm rad/s}$, respectively. For these models one might expect the post–bounce inner core, although centrifugally hung at sub–nuclear densities, to be dynamically unstable to growth of the $m = 2$ bar mode. The inner cores are not likely to be unstable to the $m = 1$ mode discussed in Reference [9], since their

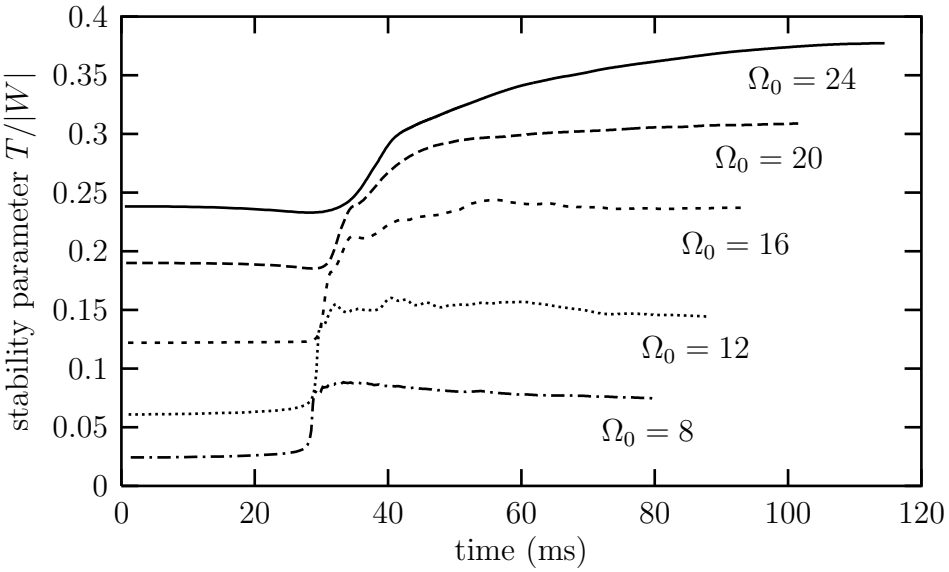

FIGURE 1. $T/|W|$ vs. t for the sequence of models (1).

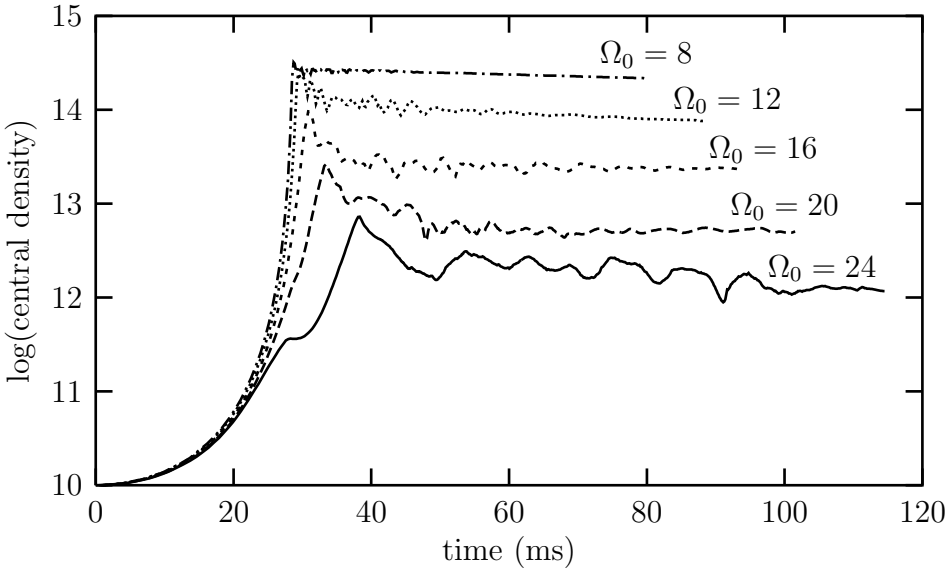

FIGURE 2. $\ln(\rho_c)$ vs. t for the sequence of models (1).

density profiles are centrally peaked. Note, however, that prior to collapse both of these models exceed the nominal threshold $T/|W| \approx 0.14$ for growth of secular instabilities. Thus, these models are unrealistic—a realistic stellar core with such a high rate of rotation would lose its axisymmetry prior to collapse. With this caveat in mind, I have forged ahead and evolved these models with the 3-D code to check for dynamical instabilities in the post–collapse inner cores. These simulations show that model Ω20 remains dynamically stable after collapse. Model Ω24 is unstable after collapse, and its inner core deforms into a bar shape.

For the model considered by Rampp, Müller, and Ruffert (RMR) [7], the pre–collapse core has an initial value for $T/|W|$ of about 0.04, well below the threshold for growth of secular instabilities. Due to the high degree of differential rotation, the material in the outer layers rotates relatively slowly. As collapse proceeds, the lack of substantial centrifugal support allows the matter in the outer layers to strongly compress the inner core. The result is that the stability parameter increases by a larger fraction than that obtained with the data sets (1). The peak value of $T/|W|$ is about 0.35, although $T/|W|$ stays above 0.27 for less than 2 ms. After bounce, the inner core relaxes and $T/|W|$ quickly settles to a value of about 0.19.

In their 3-D simulations, RMR imposed 10% random and 5% $m = 3$ density perturbations at a time of 2.5 ms before core bounce. The inner core showed $m = 2$, 3, and 4 asymmetries after bounce, but no significant enhancement in the gravitational–wave signal. Their simulations were halted at about 45 ms, approximately 15 ms after core bounce. The following question naturally arises: are the post–bounce asymmetries seen in the RMR simulation merely a transient effect caused by the asymmetrical bounce? I have carried out a 3-D simulation with the RMR initial data using 1% random density perturbations imposed at the onset of

collapse, to see if asymmetries will grow from a nearly axisymmetric bounce. I will refer to this simulation as model RMR. A second motivation for taking another look at the RMR initial data comes from the recent results in Reference [9], which suggest that a fluid body with toroidal density maximum (as occurs for model RMR both before and after collapse) can be dynamically unstable to an $m = 1$ mode for $T/|W|$ as low as ~ 0.14. The results of my simulation show that, as expected, the inner core is nearly axisymmetric immediately after core bounce. It remains axisymmetric until about 45 ms, which is the time at which RMR stopped their simulations. The dominant unstable mode that begins to grow at that time is the $m = 2$ bar mode, not the $m = 1$ mode. This occurs in spite of the fact that the stability parameter has a value of around 0.19.

Before presenting the detailed results of the 3-D simulations, I need to establish some notation. The shape of the core can be described by expanding the matter density ρ in spherical harmonics:

$$\rho(t, r, \theta, \phi) = \sum_{\ell=0}^{\infty} \sum_{m=-\ell}^{m=\ell} A_{\ell m}(t, r) Y_{\ell m}(\theta, \phi) \ . \tag{2}$$

The quadrupole formula relates the gravitational–wave amplitude to the second time derivative of the quadrupole moment of the mass distribution [12]. Inserting the expansion (2) into the quadrupole formula, we find

$$\begin{aligned} \frac{c^4 R}{2G} h_+^{TT} = \sqrt{\frac{\pi}{5}} \sin^2\Theta \langle \ddot{A}_{20} \rangle + \sqrt{\frac{2\pi}{5}} (1 + \cos^2\Theta) \, \Re(\langle \ddot{A}_{22} \rangle e^{2i\Phi}) \\ + \sqrt{\frac{8\pi}{15}} \sin\Theta \cos\Theta \, \Re(\langle \ddot{A}_{21} \rangle e^{i\Phi}) \ , \end{aligned} \tag{3a}$$

$$\frac{c^4 R}{2G} h_\times^{TT} = -\sqrt{\frac{8\pi}{15}} \cos\Theta \, \Im(\langle \ddot{A}_{22} \rangle e^{2i\Phi}) - \sqrt{\frac{8\pi}{15}} \sin\Theta \, \Im(\langle \ddot{A}_{21} \rangle e^{i\Phi}) \ , \tag{3b}$$

for the $+$ and $\times$ components of the gravitational–wave amplitude in the transverse–traceless (TT) gauge. In these formulas R, Θ, and Φ specify the distance and angular direction from the source to the observation point and $\Re$ and $\Im$ denote real and imaginary parts. The angle brackets that appear in equations (3) are defined by $\langle \ddot{A}_{\ell m} \rangle = \int dr \, r^4 \ddot{A}_{\ell m}$, which is the spatial average of the second time derivative of $A_{\ell m}$, weighted with r^2.

From equations (3) we see that only the $\ell = 2$ spherical harmonics contribute to the gravitational–wave signal in the quadrupole approximation. The coefficient A_{20} determines the oblateness of the mass distribution. Note that the space average $\langle \ddot{A}_{20} \rangle$ appears in h_+^{TT}, but not in $h_\times^{TT}$. The coefficient A_{22} corresponds to a bar–shaped deformation in the equatorial plane. Growth of this coefficient implies growth of the usual Fourier $m = 2$ bar mode. The coefficient A_{21} describes a bar–shaped deformation that is tilted out of the equatorial plane. This coefficient remains zero (apart from numerical noise) throughout the simulations, as one might

expect from symmetry considerations. Note that the coefficient A_{11}, which corresponds to the $m = 1$ mode of Reference [9], does not appear in the approximate formulas (3) for the gravitational–wave amplitude.

Figures 3 and 4 show the ratios A_{20}/ρ_0 and $|A_{22}|/\rho_0$ for model Ω24, at various radii. Here, ρ_0 is the average density at the given radius. For clarity of presentation, the results for radius $r = 60\,\mathrm{km}$ are shown with heavy curves. From Figure 3 we see that, initially, the oblateness of the core increases rapidly as matter rushes inward

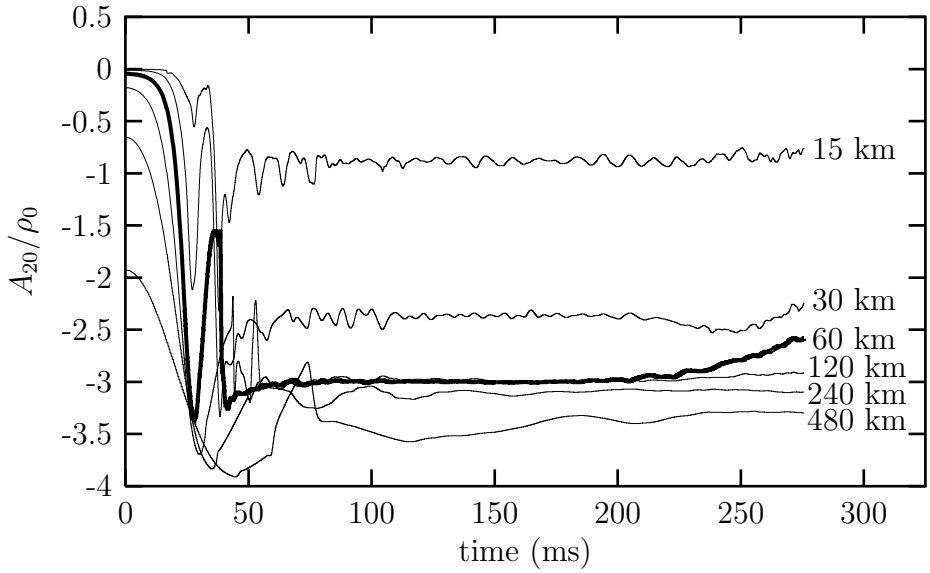

FIGURE 3. A_{20}/ρ_0 vs. t for model Ω24.

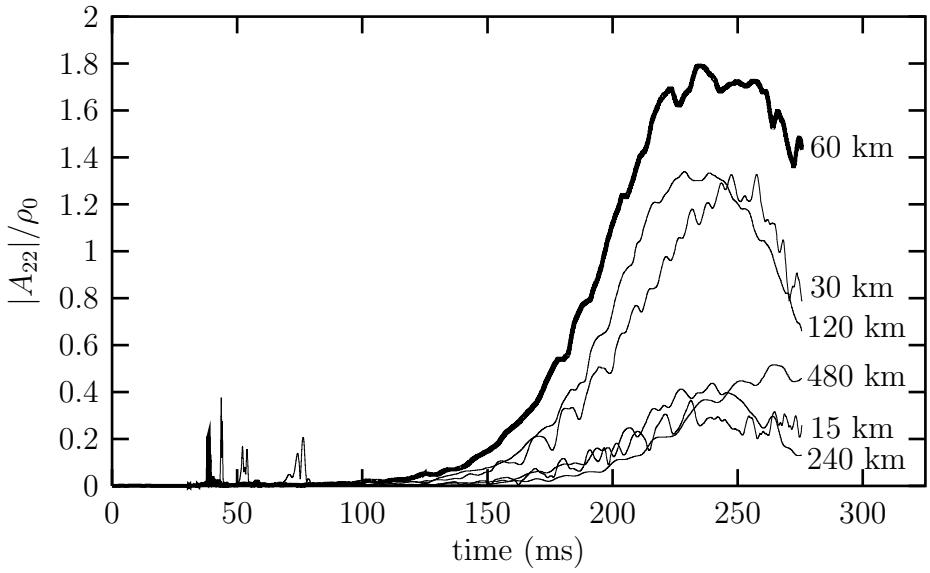

FIGURE 4. $|A_{22}|/\rho_0$ vs. t for model Ω24.

from all directions, but most rapidly along the polar regions. (A_{20} is negative for an oblate spheroid, positive for a prolate spheroid.) At ~ 28 ms the core experiences a "polar bounce" in which the matter in the polar regions is reflected off the inner core, reverses direction, and forms shock waves that propagate outward away from the equatorial plane. During the next ~ 10 ms, the oblateness of the inner core decreases as matter continues to rush in from the equator and out from the poles. At about 38 ms the core experiences an "equatorial bounce" in which the matter in the equatorial plane is reflected and forms an outwardly propagating shock wave. As the inner core relaxes, it spreads in the equatorial direction and again assumes a highly oblate shape. The oblateness remains fairly constant until near the end of the simulation, when the bar deformation becomes strong. Figure 4 shows growth of the bar mode, which begins around 100 ms. The spikes between 40 ms and 80 ms are caused by shock waves passing through the various radii. Since the shocks are not perfectly axisymmetric they produce relatively large but short–lived distortions that show up in the A_{22} coefficient. The growth rate of the bar mode for model $\Omega 24$ is $d\ln(|A_{22}|/\rho_0)/dt \approx 46/\mathrm{s}$.

A graph of the ratio $|A_{22}|/\rho_0$ for model RMR shows that the bar mode begins to grow at about 45 ms, at a rate of $d\ln(|A_{22}|/\rho_0)/dt \approx 180/\mathrm{s}$. $|A_{22}|/\rho_0$ reaches a peak value of 1.6 at ~ 70 ms. The strongest bar deformation occurs within a radius of ~ 100 km.

The graphs in Figures 5 and 6 show the gravitational–wave signals for models $\Omega 24$ and RMR, respectively. The solid curves show the + polarization amplitude (3a) as measured in the equatorial plane $\Theta = \pi/2$ at a distance of $R = 20$ Mpc (the approximate distance to the Virgo cluster). The dashed curves show the + polarization amplitude (3a) as measured along the rotation axis $\Theta = 0$ at $R = 20$ Mpc.

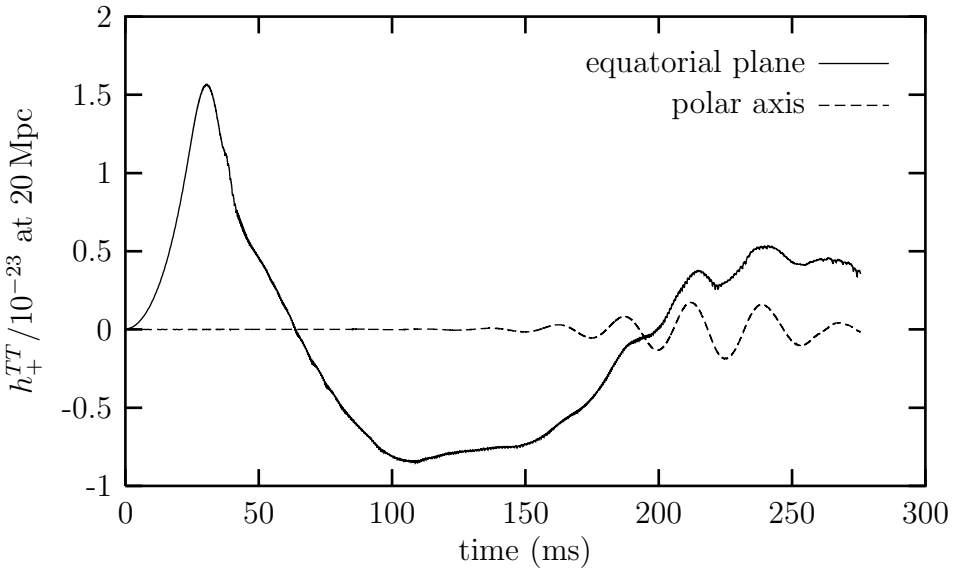

FIGURE 5. The gravitational wave amplitude for model $\Omega 24$.

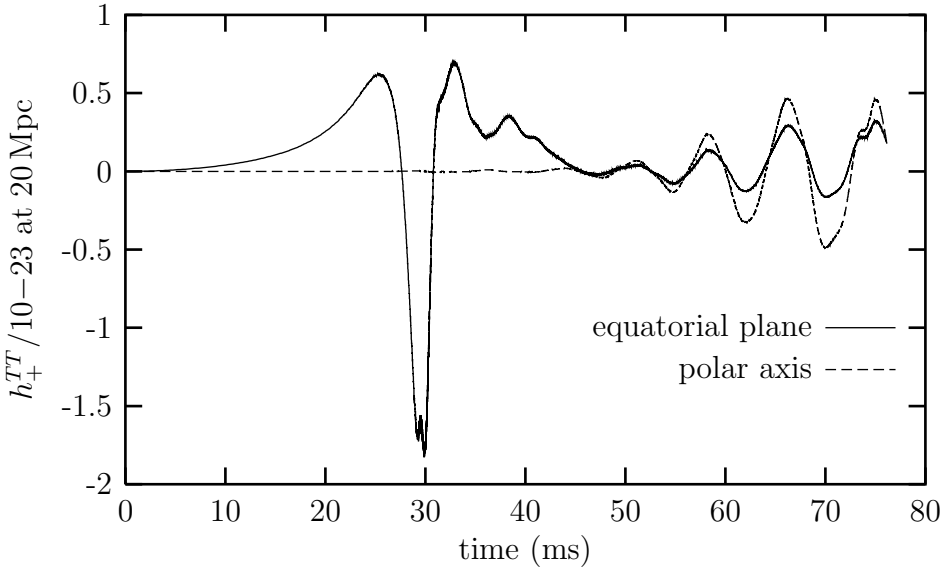

FIGURE 6. The gravitational wave amplitude for model RMR.

Since the coefficient A_{21} remains essentially zero, the $\times$ polarization amplitude (3b) at any angle is proportional to the + amplitude at $\Theta = 0$. Observe that for both models, the gravitational waves produced by the bar—the wiggles on the graphs at late times—are relatively small in amplitude compared to the gravitational waves produced by the core's (nearly axisymmetric) collapse and bounce. Fourier analysis of the gravitational–wave signal for model Ω24 shows two peaks, one around 5 Hz due to the collapse and bounce motion of the core, and the other around 40 Hz due to the rotation of the bar–shaped inner core. The total energy radiated in gravitational waves for model Ω24, up to the end of the simulation, is only a few $\times\ 10^{-9}\, M_\odot c^2$. For model RMR, the gravitational–wave signal is spread across the frequency range 25–250 Hz. The total energy radiated for this model, up to the end of the simulation, is a few $\times\ 10^{-7}\, M_\odot c^2$.

DISCUSSION

After collapse, models Ω24 and RMR are unstable to growth of the bar mode. On the other hand, model Ω20 is stable. The 3-D simulation of model Ω20 was carried out to $\sim$ 200 ms beyond core bounce, and the coefficient A_{22} showed no signs of growth. At first sight these results might seem surprising: As shown in Figure 1, the stability parameter for models Ω24 and Ω20 after core bounce exceed the nominal threshold $\sim$ 0.27 while the stability parameter for model RMR has a sustained, post–bounce value of less than 0.20. Of course, our understanding of the bar mode instability is based primarily on studies of isolated, equilibrium polytropes with Maclaurin–like rotation laws. There is little reason to believe that such a body would be a good approximation to a post–collapse stellar core and,

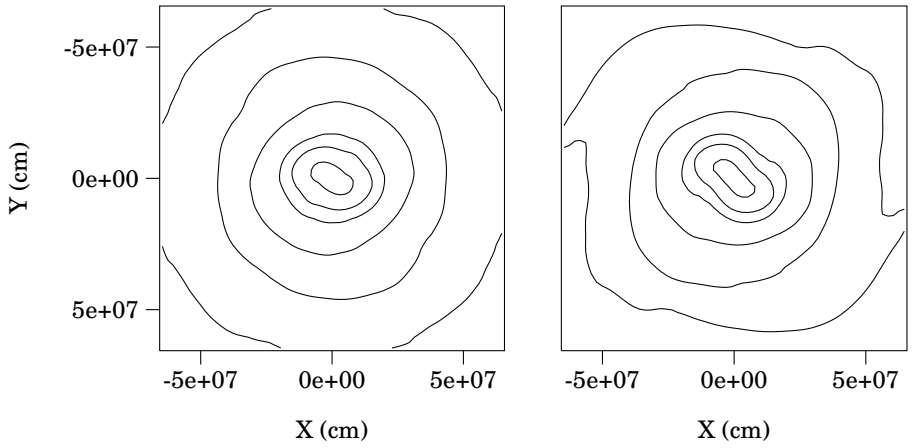

FIGURE 7. Density contours for model Ω24 at 199 ms (left) and 229 ms (right). The contour levels, in g/cm^3, are 5.0×10^9, 1.0×10^{10}, 2.0×10^{10}, 5.0×10^{10}, 1.0×10^{11}, and 5.0×10^{11}.

indeed, for the cases studied here, it is not. The value of the stability parameter for the post–collapse core is not a good diagnostic for the presence of the bar instability.

Inspection of the data for models Ω24 and RMR shows that only the most dense regions of the post–collapse core participate in growth of the bar mode. For the model Ω24 in particular, the bar deformation is contained within the region with density $\rho \gtrsim 10^{10}\,\mathrm{g/cm^3}$. Figure 7 shows contour plots of the density in the equatorial plane at 199 ms, when the bar has moderate strength, and at 229 ms, when the bar is near full strength. In the first plot, the contours below $\sim 10^{10}\,\mathrm{g/cm^3}$ are nearly circular apart from some $m = 4$ noise caused by the Cartesian grid. By the time of the second plot, the bar–shaped region with $\rho \gtrsim 10^{10}\,\mathrm{g/cm^3}$ has created "wakes" in the surrounding matter. These wakes form spiral arms that trail from the ends of the bar, and give rise to the spikes seen in the contour at $5.0 \times 10^9\,\mathrm{g/cm^3}$. Figure 8 shows the density as a function of radius in the equatorial plane for models Ω20 and Ω24. For model Ω24 the density data is taken at 161 ms, near the beginning of the bar mode growth. Note that for both models, the density has a peak in the center then levels off to a value of about $10^{10}\,\mathrm{g/cm^3}$. Beyond ~ 700 km, the density drops sharply.

Motivated by the observations above, I will define the inner core for models Ω20 and Ω24 to be the region interior to $\sim 10^{10}\,\mathrm{g/cm^3}$. Thus, we can view the post–collapse configuration as consisting of a dense inner core with $\rho \gtrsim 10^{10}\,\mathrm{g/cm^3}$ surrounded by relatively low density material. It is this inner core region that is unstable for model Ω24 and stable for model Ω20. The inner core for model RMR can be defined roughly by $\rho \gtrsim 10^{10}\,\mathrm{g/cm^3}$ as well.

Some insights into the behavior of the three models Ω20, Ω24, and RMR can be gained by defining a stability parameter for the inner core, $T_{ic}/|W_{ic}|$. The rotational kinetic energy of the inner core T_{ic} is straightforward to compute. The

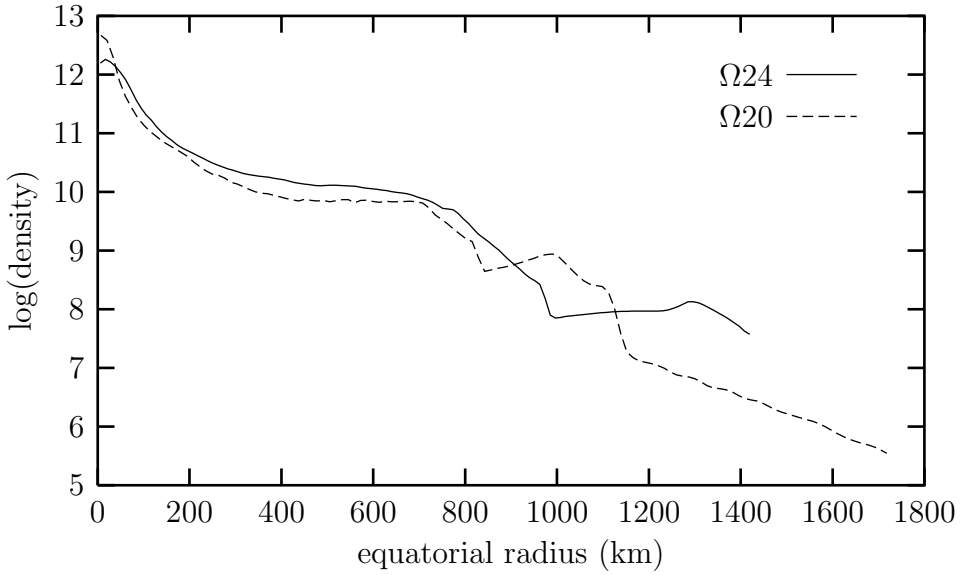

FIGURE 8. Density profile in the equatorial plane for model Ω24 at 161 ms and for model Ω20 at 182 ms.

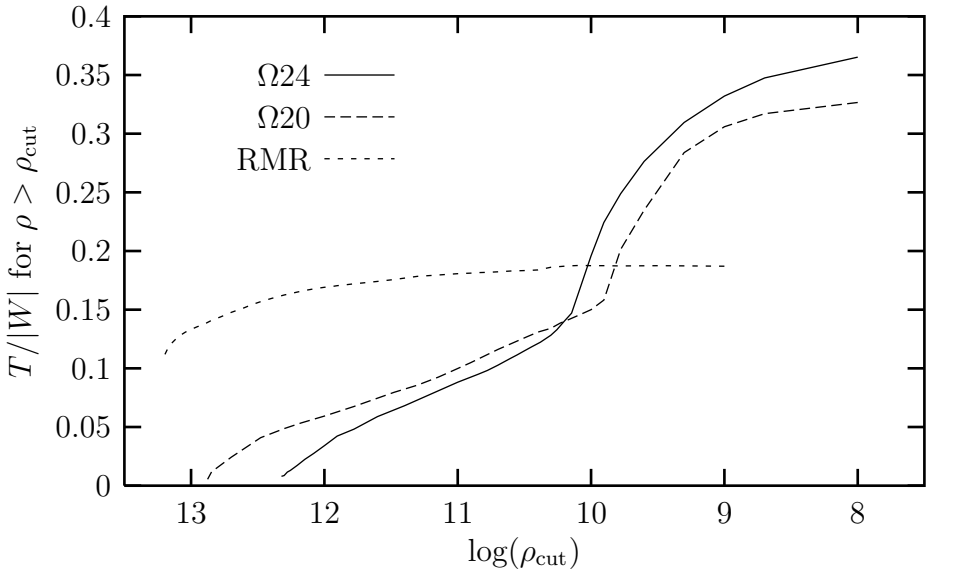

FIGURE 9. The stability parameter as a function of density cut–off for models Ω24 at 161 ms, Ω20 at 182 ms, and RMR at 52.9 ms.

gravitational potential energy W_{ic} must include the binding energy of the inner core material with itself, as well as the binding energy between the inner core material and the outer core material. The graph in Figure 9 shows the stability parameter of the region with density $\rho > \rho_{\rm cut}$, as a function of the cut–off value $\rho_{\rm cut}$, for the three models. The stability parameter for the inner core is obtained by setting $\rho_{\rm cut} \approx 10^{10}\,{\rm g/cm^3}$. The graph shows that for model Ω20, $T_{ic}/|W_{ic}| \approx 0.15$ while for

models Ω24 and RMR, $T_{ic}/|W_{ic}| \approx 0.19$. Based on these results, we might expect that model RMR is less stable than model Ω20. Indeed, as the 3-D simulations show, RMR is unstable and Ω20 is stable. Perhaps the more interesting question is this: Why are the inner cores for Ω24 and RMR unstable, given the fact that the values for their stability parameters are well below 0.27? The explanation might simply be that the post–collapse inner cores are not equilibrium polytropes with Maclaurin–like rotation laws, so the threshold for dynamical instability might be far different from 0.27. Another explanation might be that a post–collapse inner core is not isolated, and coupling to the outer core material can drive the bar instability. If this is correct, then growth of the bar mode is a secular process, as discussed for example by Schutz [13]. Note that for isolated, equilibrium polytropes with Maclaurin–like rotation laws, the threshold for growth of the secular instability is about 0.14. The inner core stability parameters for Ω24 and RMR are well above this threshold. On the other hand, the stability parameter of the inner core for model Ω20 is very close to the threshold.

ACKNOWLEDGMENTS

I would like to thank John Blondin for helpful discussions and for his work on the numerical codes. This research was supported by NSF grant PHY-0070892. Computer resources were provided by the North Carolina Supercomputing Center.

REFERENCES

1. Yamada, S., and Katsuhiko, S., *Ap. J.* **450**, 245–252 (1995).
2. Zwerger, T., and Müller, E., *Astron. Astrophys.* **320**, 209–227 (1997).
3. Bethe, H.A., *Rev. Mod. Phys.* **62**, 801–866 (1990).
4. Müller, E., and Janka, H.-T., *Astron. Astrophys.* **317**, 140–163 (1997).
5. See for example Tauris, T.M., and van den Heuvel, E.P.J., to appear in the proceedings of the IAU Colloq. 177 "Pulsar Astronomy—2000 and Beyond". (astro-ph/0001015)
6. Burrows, A., and Hayes, J., *Phys. Rev. Lett.* **76**, 352–355 (1996).
7. Rampp, M., Müller, E., and Ruffert, M., *Astron. Astrophys.* **332**, 969–983 (1998).
8. Tassoul, J., *Theory of Rotating Stars*, Princeton: Princeton University Press, 1978.
9. Centrella, J.M., New, K.C.B., Lowe, L.L., and Brown, J.D., submitted to *Ap. J. Lett.* (astro-ph/0010574). See also New, K.C.B., this volume.
10. Colella, P., and Woodward, P.R., *J. Comput. Phys.* **54**, 174–201 (1984).
11. Heger, A., Langer, N., and Woosley, S.E., Ap. J. **528**, 368–396 (2000).
12. Misner, C.W., Thorne, K.S., and Wheeler, J.A., *Gravitation*, San Francisco: W.H. Freeman, 1973.
13. Schutz, B.F., "Problems in Astrophysical Fluid Dynamics", in *Fluid Dynamics in Astrophysics and Geophysics*, edited by N.R. Lebovitz, AMS Lectures in Applied Mathematics **20**, Providence, 1983, pp. 99–140.